Effect of β-Li₃N phase, Li₂O addition and thermal treatment on the hydrogen sorption behavior of Li₃N

L. Fernández-Albanesi [a,c], P. Arneodo Larochette [a,b,c], F.C. Gennari [a,b,c,*]

[a] Instituto Balseiro (Universidad Nacional de Cuyo), Argentina
[b] Consejo Nacional de Investigaciones Científicas y Técnicas (CONICET), Argentina
[c] Centro Atómico Bariloche, 8400 S.C. de Bariloche, Río Negro, Argentina

ABSTRACT

The hydriding of Li₃N to LiNH₂ is investigated to clarify the influence of the β-Li₃N phase, the addition of Li₂O and the thermal treatment of Li₃N on the hydrogen storage properties of the Li–N–H system. As-milled Li₃N displays fast initial absorption that is attributed to the formation of β-Li₃N nanograins, the increase of the surface area, and the presence of surface defects induced by mechanical milling. However, further hydrogen absorption is retarded in comparison with the as-received sample due to the presence of the β-Li₃N phase formed during milling. Thus, commercial Li₃N exhibits the highest hydrogen storage capacity in the first cycle in comparison with as-heated Li₃N and as-milled samples. In the case of Li₂O addition, no interaction with Li₃N was detected. The addition of LiH to the commercial Li₃N, as-milled Li₃N and Li₃N–Li₂O influences only the stability of the samples under hydrogen cycling. The hydrogen absorption/desorption behavior is mainly controlled by the amount of β-Li₃N formed during milling, while at long times the microstructure has a minor effect.

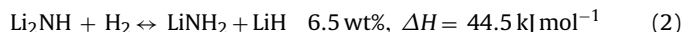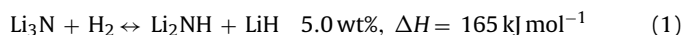© 2011 Elsevier B.V. All rights reserved.

1. Introduction

Considering the increasing of both environmental pollution and consumption of fossil energy resources, alternative energy carriers will become essential for the future industrial society. Hydrogen emerges as an excellent candidate mainly for its abundance and nonpolluting nature. However, its utilization as an energy carrier for a sustainable economy requires overcoming several scientific and technological limitations, in particular the development of suitable hydrogen storage media [1].

Storing hydrogen as a solid hydride material is attractive, being both a safe and an efficient strategy. Its volumetric density may be higher than the densities of both compressed and liquid hydrogen. In the last 30 years, substantial progress has been made in optimizing the thermodynamic/kinetic properties of several metal–hydrogen systems. Unfortunately, advances originated in the study of conventional reversible hydrides failed to propose a solution to the problem of hydrogen storage [1–3]. While some materials such as MgH₂ meet the requirement of gravimetric capacity (7.6 wt% of H), their application is limited due to high thermodynamic stability (for MgH₂, $\Delta H \cong 70$–$74\,\mathrm{kJ\,mol^{-1}\,H_2}$), resulting

in high temperatures for hydrogen desorption at atmospheric pressure.

The family of complex hydrides (alanates AlH_4^-, amides NH_2^- and borohydrides BH_4^-) formed by light metals of groups I–III (Li, Na, Mg) are an alternative to the traditional hydrides. They have excellent gravimetric densities (between 6 and 18 wt% of H) and volumetric densities ($>100\,\mathrm{kg\,m^{-3}}$) [4,5]. In particular, the Li–N–H system has received special attention in the recent years, starting with the report of Chen et al. [6]. These authors proposed that the Li₃N nitrure absorbs hydrogen reversibly according to the following reactions:

$$Li_3N + H_2 \leftrightarrow Li_2NH + LiH \quad 5.0\,\mathrm{wt\%}, \quad \Delta H = 165\,\mathrm{kJ\,mol^{-1}} \qquad (1)$$

$$Li_2NH + H_2 \leftrightarrow LiNH_2 + LiH \quad 6.5\,\mathrm{wt\%}, \quad \Delta H = 44.5\,\mathrm{kJ\,mol^{-1}} \qquad (2)$$

Hydriding was accomplished at 0.3 MPa of hydrogen in the temperature range of 170–210 °C for the first step, and about 255 °C for the second step. This last reaction provides a good theoretical hydrogen storage capacity, with a relatively low enthalpy of reaction and a reasonable hydrogen pressure of about 0.1 MPa at 285 °C. Furthermore, additional studies have shown that hydrogen desorption from the LiNH₂ amide (reverse of reaction (2)) proceeds in two steps [7–11]. First, the amide decomposes to release ammonia (NH₃, reaction (3)), which subsequently reacts with the LiH hydride to form hydrogen and LiNH₂ (reaction (4)).

$$2LiNH_2 \rightarrow NH_3 + Li_2NH \qquad (3)$$

* Corresponding author at: Centro Atómico Bariloche (CNEA), R8402AGP, S.C. de Bariloche, Río Negro, Argentina. Tel.: +54 2944 445118; fax: +54 2944 445190.
  E-mail address: gennari@cab.cnea.gov.ar (F.C. Gennari).

$$NH_3 + LiH \rightarrow LiNH_2 + H_2 \tag{4}$$

Ichikawa et al. [8] confirmed the presence of NH_3 as a gaseous intermediate during decomposition of $LiNH_2$–LiH. Interestingly, they showed that the quantity of evolved NH_3 decreases sharply when $LiNH_2$ and LiH react in a 1:2 ratio or when the $LiNH_2$–LiH mixture is ball milled. In an independent study [9], it has been demonstrated that reaction (4) is ultrafast and can take place in the order of microseconds, LiH being the responsible of the NH_3 capture.

Several studies have focused on the hydrogen storage properties of the $LiNH_2$–LiH system, whereas there are fewer works concerning the hydriding process starting from Li_3N [12–15]. Hu and Ruckenstein [12] have reported that partially oxidized Li_3N (Li_2O–Li_3N) is able to absorb reversibly 5 wt% of hydrogen in only 3 min at 180–200 °C. The combination of partial oxidation of Li_3N and the high hydriding/dehydriding temperature was proposed to be the responsible of the improved hydrogen storage observed (fast kinetics and good stability). According to the authors, the presence of Li_2O avoids the generation of hot spots during the hydrogen absorption; the estimated amount of Li_2O was 17 wt%. In another work, the same authors [13] have shown the effect of the heat pretreatment of Li_3N on the hydrogen storage capacity and stability. Despite commercial Li_3N quickly absorbed 5.5 wt% of hydrogen at 230 °C, additional 50 h were required for 2.5 wt% of hydrogen. In contrast, Li_3N preheated at 400 °C in vacuum for 4.5 h absorbed 3 wt% at 230 °C and required only 5 h for extra 6.5 wt% of hydrogen. The same authors [14] demonstrated that the dehydriding of hydrided Li_3N at 400 °C under vacuum induces deactivation of Li_3N as a consequence of sintering. These results are contradictory in relation with the effect of thermal treatment on hydrogen absorption. A recent work has focused on the hydriding of commercial Li_3N, milled Li_3N and Li_3N doped with Li_2O [15]. The as-milled Li_3N material showed the lowest onset temperature for hydrogenation and better cycling properties than the unmilled Li_3N. The addition of Li_2O did not enhance the hydrogen storage performance of commercial Li_3N. Li_2O remains as a separate phase without evidence of interaction with Li_3N.

Recently, experimental evidence and theoretical calculations strongly suggested that the reaction pathways for hydriding/dehydriding Li_3N are more complex than that represented by Eqs. (1) and (2) [16–20]. David et al. [16] have reported a series of non-stoichiometric phases with composition $Li_{2-x}NH_{1+x}$ in the decomposition product of hydrided Li_3N. Indeed, both Li_2NH and $LiNH_2$ are the end members of this series with values of $x = 0$ and $x = 1$, respectively. Weidner et al. [17] have detected the formation of a cubic non-stoichiometric "quasi-imide" phase during deuterium absorption of Li_3N at low pressure, with a composition-dependent lattice parameter. In this last study, the simultaneous formation of Li_4ND was observed as a function of the deuterium content, and the consumption of Li_3N was higher than that suggested by Eq. (1). Chandra et al. [18] have also observed that hydrogenation of Li_3N proceeds along a more complex mechanism than reactions (1) and (2), involving two intermediary phases: Li_4NH and a new solid-solution cubic phase of $Li_{2-x}NH_{1+x}$, which were observed at hydrogen concentrations between 3.2 wt% H and 8.1 wt%. Moreover, Huq et al. [19] have studied the deuteration of α-Li_3N using in situ neutron diffraction. They observed a change in the unit cell volume of the Li_2NH during absorption and desorption at 250 °C that indicates a possible $Li_xND_{(3-x)}$ stoichiometry during cycling. Two cubic phases with slightly different lattice parameters were formed after cooling the sample to room temperature. A recent study using neutron diffraction during the in situ deuteration of Li_3N has shown different final phases as a function of pressure [20]. At 0.5 MPa, non-stoichiometric phases were not detected, and the reaction proceeded to the formation of amide

plus LiH. However, at lower pressures, a cubic phase with a large variation in lattice parameter was observed. The authors emphasize the relevance of clarifying whether the formed phases have composition $Li_{2+y}NH$ or $Li_{2+y}NH_{1-y}$. Simultaneously, the stability of the different intermediate phases between Li_2NH and $LiNH_2$ has been studied using density functional theory DFT, providing additional insight on the predominant phase in the hydrogenation and dehydrogenation process [21,22].

All above mentioned works were addressed to study the α-Li_3N hydriding/dehydriding reactions. Whereas Li_3N is the only stable binary alkali metal nitride in the Li–N system [23], α-Li_3N is the stable phase at room temperature and ambient pressure. Its hexagonal structure consists of Li_2N layers, widely separated and connected by one lithium atom per unit cell occupying a site between the nitrogen atoms in adjacent layers [24]. At around 0.6 GPa and room temperature, α-Li_3N transforms into a layered hexagonal structure (β-Li_3N) with BN-like honeycomb LiN layers [25]. Although the β-Li_3N structure retains some key aspects of the α-Li_3N, its Li–N layers switch from a composition $[Li_2N]$ to $[LiN]$ as nitrogen atoms are shifted from a simple hexagonal packing to hexagonal eutaxy [24]. Huq et al. [26] have presented a detailed structural study of Li_3N in the temperature range of 250–400 °C using neutron powder diffraction. They observed the progressive transformation from β to α-Li_3N above 200 °C. Moreover, β-Li_3N presented a high thermal stability, remaining 2.5 wt% untransformed at 400 °C. Considering that commercial Li_3N normally contains both α and β phases, it is interesting to study the possible effect of β-Li_3N presence on the hydrogen storage properties of Li_3N.

In this work, we analyze the role of the β-Li_3N phase, the Li_2O presence, and the thermal treatment under vacuum on the hydrogen storage capacity and the hydriding/dehydriding kinetics of Li_3N. We obtain evidence of the formation of a $Li_{2-x}NH_{1+x}$ non-stoichiometric phase under specific experimental conditions, confirming the complex nature of the Li_3N hydriding/dehydriding process. Moreover, the influence of temperature and milling time on the β to α-Li_3N transition is evaluated.

2. Experimental

2.1. Synthesis of the materials

Powders of Li_3N (>99.9% of purity, Aldrich), Li_2O (>97% of purity, Aldrich) and LiH (>95% of purity, Fluka) were used as starting materials. Two sets of samples were prepared to study the effect of different variables on the hydriding/dehydriding behavior of Li_3N. The first group of samples consists of as-received Li_3N powders (commercial, referred as LN), as-milled Li_3N (m-LN), as-heated Li_3N (h-LN) and as-milled mixture of Li_3N with 17 wt% of Li_2O (m-LNO). The time of milling (X) is referred to as m-LNX or m-LNOX, respectively. The second group of samples is formed by LN, m-LN20 and LNO samples which were milled with 27 wt% of LiH (1.6 mol%) for 2 h, 2 h and 5 h, respectively. The final samples are hereafter indicated as LN–LH2, m-LN20–LH2 and m-LNO–LH5, respectively. Ball milled samples were prepared using planetary ball milling (Fritsch P-6) with a ball to powder ratio of 40:1 in a hardened steel vial under 0.1 MPa of argon. The as-heated Li_3N sample was obtained after thermal treatment under vacuum at 400 °C for 4 h. All sample handling was done in an MBraum Unilab argon-filled glove box, with oxygen and moisture levels lower than 1 ppm.

2.2. Material characterization

The as-prepared and as-cycled samples were characterized by means of powder X-ray diffraction measurements (PXRD, Philips PW 1710/01 Instruments), infrared spectra collection (FTIR Perkin

Elmer Spectrum 400), scanning electron microscopy observations combined with EDS (SEM 515, Philips Electronic Instruments with energy dispersive X-ray spectroscopy), N_2 sorption isotherms (Micromeritics ASAP 2020) and differential scanning calorimetry analysis (DSC TA 2910 calorimeter).

Structural information of the different samples was obtained by PXRD analysis (CuKα radiation, graphite monochromator) and FTIR analysis. During the PXRD data collection all the samples were maintained under Ar atmosphere using a tightly sealed sample holder to prevent the reaction between samples and air. The formation degree of β-Li$_3$N from α-Li$_3$N phase, A (in %), was calculated from XRD measurements using the equation

$$A_{\beta\text{-Li}_3\text{N}} = \frac{I_{\beta\text{-Li}_3\text{N}}}{I_{\beta\text{-Li}_3\text{N}} + I_{\alpha\text{-Li}_3\text{N}}} \times 100 \tag{5}$$

where I represents the intensity of the most intense reflections of α-Li$_3$N or β-Li$_3$N. Crystallite size of the α and β-Li$_3$N phases were estimated from the most intense diffraction peaks by the Scherrer equation. For IR spectroscopy measurements, the selected samples were grounded with dry KBr under purified argon atmosphere and pressed to pellets. Solid-state IR spectra were obtained in the range of 450–4000 cm^{-1} using a specially designed cell. Handling was done inside the glove box to avoid contact with air.

Morphological and textural characterizations were performed *via* SEM observations and N_2 sorption measurements. For the SEM, the samples were dispersed on stick-mounted holders and introduced into hermetic plastic recipients in the argon-filled glove box to minimize the material's surface exposure to oxygen and humidity. Textural measurements were performed at liquid nitrogen temperature to determine the specific surface area (SSA) based on the Brunauer–Emmett–Teller (BET) method, pore volume and size distribution. Before measurements, the samples were evacuated at 150 °C overnight.

The thermal behavior of the samples was studied by DSC using a heating rate of 5 °C min^{-1} and an argon flow rate of 122 ml min^{-1}. About 10 mg of sample was loaded into aluminum capsules hermetically closed in a glove box under a purified argon atmosphere. The heat associated with the α to β-Li$_3$N phase transition was estimated from DSC curves using the peak area and the mass of each sample.

Isothermal hydrogen sorption curves were obtained using modified Sieverts-type equipment, coupled with a mass flow controller. Isothermal hydrogen absorption curves were measured at 200 °C with a hydrogen pressure of only 0.7 MPa (2 h) and then switched to 3.0 MPa (additional 5 h). In some cases the first stage at 0.7 MPa is not performed. Isothermal hydrogen desorption curves were obtained at 250 °C under vacuum (0.025 MPa). Each sample was heated up to the reaction temperature under vacuum and kept at this temperature for 30 min before measuring the hydrogen absorption/desorption reaction. For non-isothermal absorption measurements, the sample was heated at 5 °C min^{-1} from room temperature to 200 °C at 3.0 MPa of hydrogen pressure. The reported values of hydrogen uptake/release are expressed as wt% with respect to the amount of Li$_3$N in the starting sample, to facilitate the comparison between the sorption curves.

3. Results and discussion

3.1. Structural and microstructural characteristics of the Li$_3$N samples

Fig. 1 shows the XRD patterns of as-received Li$_3$N (LN), as-milled Li$_3$N (m-LN20), as-heated Li$_3$N (h-LN) and as-milled Li$_3$N–Li$_2$O mixture (m-LNO5). The commercial LN exhibits the coexistence of both α-Li$_3$N (main phase, stable) and β-Li$_3$N (metastable), with the
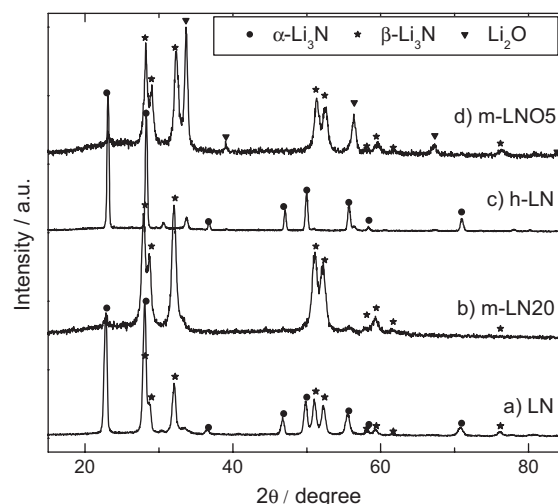

Fig. 1. PXRD patterns of: a) LN; b) m-LN20; c) h-LN; d) m-LNO5.

simultaneous presence of minor amounts of Li$_2$O. The sample m-LN20 shows mainly the peaks attributable to β-Li$_3$N. This indicates the almost complete α to β-Li$_3$N transition after milling for 20 h. In contrast, the complete transition of β to α-Li$_3$N phase as well as the crystallization of Li$_2$O is observed after a thermal treatment at 400 °C for 4 h (h-LN). Moreover, milling of the Li$_3$N–Li$_2$O mixture for 5 h also induces the transition of α to β-Li$_3$N phase (m-LNO5 sample). The peaks of Li$_2$O are clearly identified and no evidence of interaction between Li$_3$N and Li$_2$O is detected.

The SEM examinations of the different samples reveal that the commercial Li$_3$N is formed by agglomerates (assemblages of particles) with a wide size distribution: ~6% of the agglomerates between 100 and 200 μm, 21% between 20 and 50 μm and 62% being <20 μm. A detail of the surface of these agglomerates shows several particles of 1–2 μm (Fig. 2a), which are aggregated in secondary particles of 10 μm. After ball milling for 20 h, the agglomerate size distribution is modified: ~12% of the agglomerates between 100 and 200 μm, 23% between 50 and 100 μm and 54% between 20 and 50 μm. These results suggest that additional large agglomerates form due to cold welding after a prolonged milling time. The surface of these agglomerates (Fig. 2) shows particles of different sizes. In comparison with as-purchased Li$_3$N (Fig. 2a), the as-milled Li$_3$N consists of smaller particles (<0.5 μm, Fig. 2b) that are relatively homogeneous in shape and size. Moreover, the h-LN sample presents a lower fraction of small size agglomerates than the LN sample: 5% of the agglomerates between 100 and 200 μm, 27% between 20 and 50 μm and 48% being <20 μm. The surface of the agglomerates shows large pores (Fig. 2c) in comparison with the commercial Li$_3$N (Fig. 2a).

Table 1 summarizes the crystallite sizes, the SSA and the equivalent particle size of the different Li$_3$N samples. It can be seen that the crystallite size of both α and β-Li$_3$N has been reduced to less than

Table 1
Microstructural characteristics of as-received and as-prepared Li$_3$N samples.

	Crystallite size (nm)		SSA (m^2 gr^{-1})	Equivalent particle size (μm)[a]
	α-Li$_3$N	β-Li$_3$N		
LN	21	18	4	1.15
m-LN20	14	14	5	0.92
m-LNO5	14	14	3	1.53
h-LN	33	–	4	1.15

[a] The equivalent particle size was calculated from SSA assuming spherical particles.
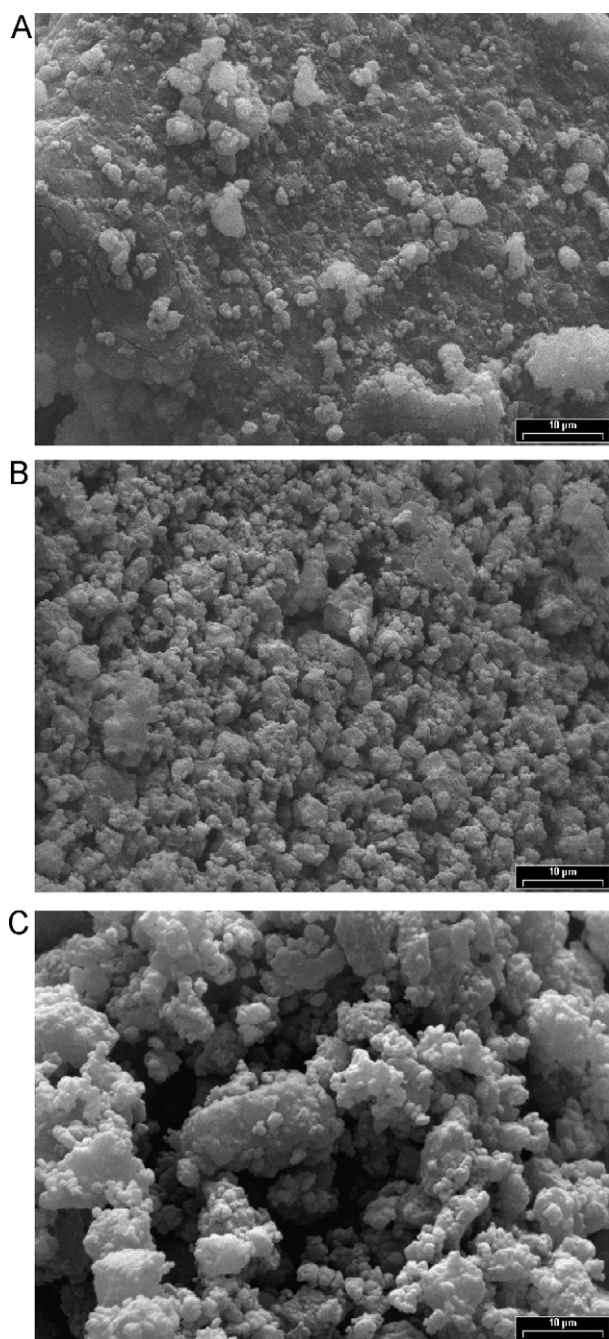
Fig. 2. SEM images of the as-prepared samples: a) LN; b) m-LN20; c) h-LN.

Fig. 3. DSC curves of: a) LN; b) m-LN5; c) m-LN10; d) m-LN20; e) m-LNO5.

15 nm after 20 h of milling. In contrast, thermal treatment notably increases the crystallite size to 33 nm. It must be remarked that the SSA of Li_3N increases slightly after milling. The equivalent particle size calculated for the LN and m-LN samples is in agreement with the SEM examination. In addition, the equivalent particle size calculated from the SSA is much larger than the crystallite size estimated from XRD peak broadening. This indicates that each Li_3N particle identified by SEM contains several crystallites.

Thermal stability of the LN, m-LN and m-LNO samples was investigated using DSC measurements (Fig. 3). All samples display a similar thermal behavior, characterized by the presence of an exothermic peak that presents two interesting features. First of all, the peak temperature increases as milling time progresses from the LN sample (250 °C, which contains the β-Li_3N phase) to the m-LN20 sample (344 °C, which consists mainly of β-Li_3N). Secondly,
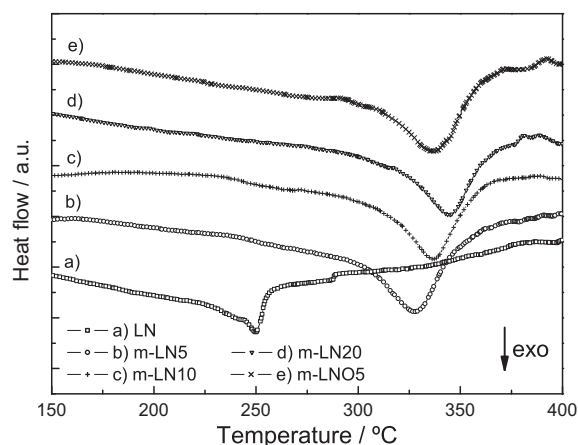
the peak area increases with respect to the LN sample due to milling, but it seems to become constant after 5 h of milling. On the basis of Fig. 1, the exothermic peak observed for the different samples can be associated with the β to α-Li_3N phase transition. Considering that the endothermic peak area is directly correlated with the proportion of the β-Li_3N phase in the sample, an estimation of the heat flow as a function of milling time was done (see Table 2). The peak area increases from about 55 J g^{-1} for LN to 154 J g^{-1} for the m-LN20 sample, being about 155 J g^{-1} after 5 h of milling. Moreover, the DSC curve for the m-LNO5 sample also presents the exothermic peak due to the Li_3N phase transformation but at a lower temperature, similar to that corresponding to m-LN10. These values reveal that the proportion of the β-Li_3N metastable phase increases respect to the α-Li_3N due to milling, but it remains practically constant after 5 h of milling.

Furthermore, we can also evaluate the α to β-Li_3N phase transformation by estimation of the formation degree of β-Li_3N (see Eq. (5)) from XRD measurements. To complete the analysis, additional samples were prepared by milling during different times, or milling followed by heating. Table 2 summarizes the formation degree of β-Li_3N calculated for several samples. Commercial Li_3N possesses about 30% of β-Li_3N phase. After milling for 5 h the fraction of β-Li_3N phase is 90% and it remains practically constant after 20 h of milling. Total transformation from α to β-Li_3N phase is not reached under the experimental milling conditions, probably due to the powders sticking in the milling chamber. The m-LN20 heated at 225 °C for 5 h shows about 68% of β-Li_3N phase, indicating that partial transition from β to α-Li_3N phase occurs slowly at this temperature. Analyses performed using EDS on m-LN5 and m-LN20 demonstrate that the Fe amount is lower than 1 at%. This result indicates that Fe contamination is not a necessary factor to induce the α to β-Li_3N phase transition during milling, as it was previously suggested [27]. Finally, the values of heat flow obtained from DSC measurements are in agreement with the trends found by XRD (Table 2).

Table 2
Summary of the DSC results and formation degree of β-Li_3N obtained from XRD.

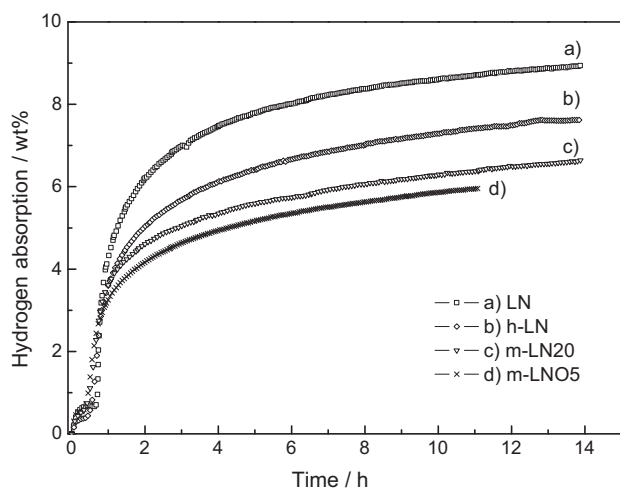| Samples	Peak temperature (°C)	Peak area (J g^{-1})	$A_{\beta\text{-}Li_3N}$
LN	250	55	30
m-LN1	–	–	76
m-LN5	328	155	90
m-LN10	337	152	92
m-LN20	344	154	93
m-LNO5	337	144	90
m-LN20 heated at 225 °C, 5 h	–	–	68

Fig. 4. Hydrogen absorption kinetics of: a) LN; b) h-LN; c) m-LN20; d) m-LNO5. Non-isothermal absorption from room temperature to 200 °C under 3.0 MPa of hydrogen pressure.

3.2. Hydriding/dehydriding behavior of Li_3N samples

The hydrogen absorption behavior of the different Li_3N samples was investigated under non-isothermal conditions (3.0 MPa of hydrogen pressure, final temperature 200 °C). All samples absorb about 3 wt% in the first hour, while additional hydrogen uptakes involve longer times, of about 12 h (Fig. 4). In previous works, it was experimentally observed that $LiNH_2$ and Li_2NH were formed at similar rates, which suggests that both phases were produced from the reaction between Li_3N and H_2 gas in addition to the conversion of Li_2NH to $LiNH_2$ (reaction (2)) [19]. We believe that a similar situation occurs during our Li_3N hydriding experiments and thus it is not possible to correlate each stage with reaction (1) or (2). After 12 h of hydriding, the best kinetics was observed for commercial LN, which displays the highest hydrogen content of 8.9 wt%. The final hydrogen storage capacity for m-LNO5, m-LN20 and h-LN was about 6.0, 6.5 and 7.5 wt%, respectively. Thus, for milled- and commercial-LN materials there is a correlation between the β-Li_3N fraction in the starting sample (Table 2) and the final hydrogen storage capacity obtained (Fig. 4). In the case of h-LN sample, the absence of β-Li_3N might suggest superior hydrogen storage capacity. However, the thermal treatment increases both the crystallite size of Li_3N and the agglomerate size distribution respect to commercial LN, negatively influencing its hydrogen reactivity [16].

Accordingly, hydrogen absorption/desorption cycling was performed for the best two samples after the first absorption cycle (Fig. 4), i.e. LN and h-LN. The amount desorbed from these samples at 250 °C was 3 and 1.3 wt%, respectively, after 3 h under vacuum. Successive hydrogen absorption (200 °C) and desorption (250 °C) cycling leads to a progressive reduction in the reversible hydrogen storage capacity for the LN sample, with 2.7 wt% of hydrogen absorbed after the 5th cycle. The loss of reversibility observed may be partially associated with the formation of NH_3, in agreement with previous works [7,8,10,11].

To compare the morphological and microstructural changes of the samples as consequence of cycling, SEM observations and surface area determinations were carried out. Fig. 5 shows the surface morphology of the as-cycled LN (Fig. 5a, 5th absorption cycle), m-LN20 (Fig. 5b, first absorption cycle) and h-LN (Fig. 5c, 5th absorption cycle) samples. The surface of these agglomerates displays several particles between 1 and 2 μm, which are aggregated in secondary particles of different sizes. A comparison with the morphology of the powders presented in the Fig. 2 shows that the surface roughness has clearly changed for the LN and m-LN
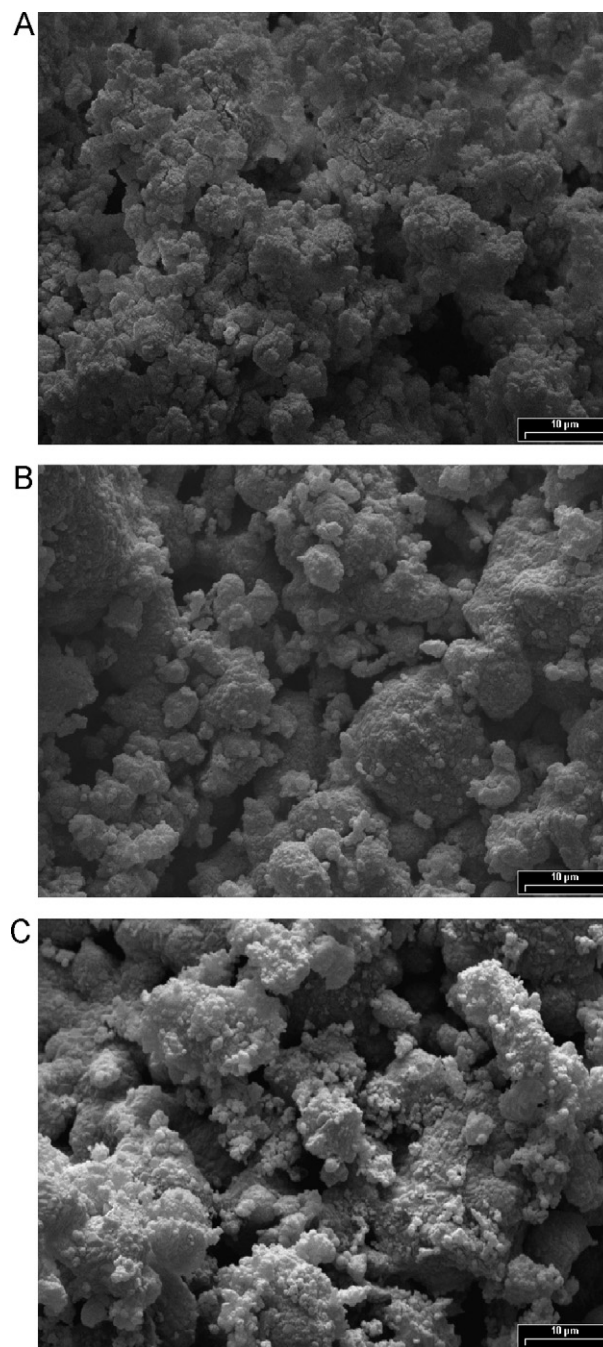

Fig. 5. SEM images of as-cycled samples: a) LN; b) m-LN20; c) h-LN.

samples, while it looks similar for the h-LN material after cycling. However, these modifications are not reflected in the values of the specific surface area: the three samples have BET areas of about of $2\,m^2\,g^{-1}$ after successive hydrogen cycling.

To obtain additional insight on the hydriding/dehydriding process, Fig. 6 shows PXRD patterns of the samples after cycling. During the first absorption for the LN and m-LN samples, both $LiNH_2$ and Li_2NH phases are formed, whereas α-Li_3N (curve a) and β-Li_3N (curve d) phases remain unhydrided. Note that the β-Li_3N phase is still present after 12 h of heating at 200 °C. Moreover, after the 5th hydrogen absorption cycle, PXRD patterns for the LN and h-LN samples show the formation of $LiNH_2$, minor amounts of Li_2NH and remnant α-Li_3N (curve c and e, respectively), without clear differences between both samples after cycling. Li_2O is also detected, probably due to the crystallization of Li_2O present in the
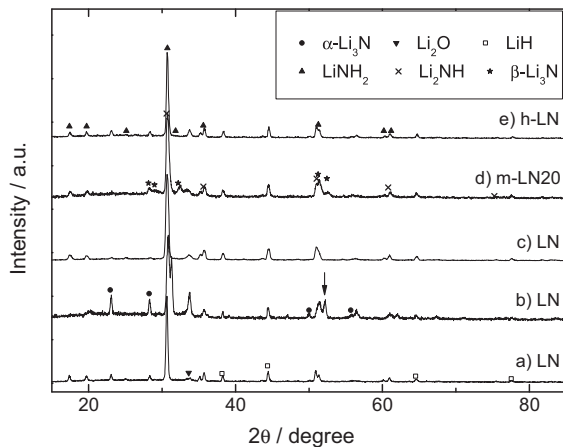
Fig. 6. PXRD patterns of: a) first absorption of LN; b) first desorption after absorption (a) of LN; c) 5th cycle of absorption of LN; d) first absorption of m-LN20; e) 5th cycle of absorption of h-LN. Non-isothermal absorptions were performed from room temperature to 200 °C, under 3.0 MPa of hydrogen pressure. Isothermal desorption was performed at 250 °C, under 0.02 MPa of hydrogen pressure.

commercial Li_3N (Fig. 1, curve a) as a consequence of the prolonged thermal treatment. Moreover, the formation of a $Li_{2-x}NH_{1+x}$ phase [18] is identified from PXRD for LN after the first hydrogen desorption (indicated by an arrow in curve b, Fig. 6). Probably, minor amounts of Li_4NH are also formed, as it is inferred from the incipient peak at about $2\theta = 20.2°$ [28]. Our results are in agreement with recent works, which show that the Li_3N hydriding/dehydriding mechanism is a more complex process than that represented by Eqs. (1) and (2) [16–20].

The hydrogen storage capacity as well as the hydrogen absorption rate of the Li_3N samples presented in Fig. 4 differ of those obtained by Langmi et al. [15]. They showed that milled Li_3N has better hydrogen cycling properties than unmilled Li_3N, whereas the addition of Li_2O does not modify the absorption behavior. However, no mention was made to the presence of β-Li_3N in the milled Li_3N. In order to analyze the different performance of commercial and milled Li_3N samples during the first hour of hydrogen absorption and to relate it with the presence of the β-Li_3N phase, isothermal measurements at 200 °C under 0.7 MPa of hydrogen pressure (Fig. 7) were carried out. As-purchased LN displays superior hydrogen storage, while m-LN5 and m-LNO samples absorb less hydrogen under the same experimental conditions. Moreover, the highest hydriding rate is obtained for the m-LN5 sample after the first 10 min. Then, two opposite factors seem to con-
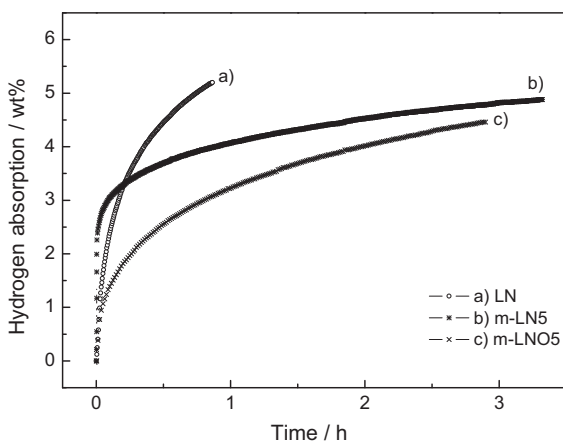
trol the hydriding process at different times. At the beginning of hydrogen absorption, the kinetic behavior is strongly influenced by the microstructural modifications introduced by milling. The milling process produces significant internal, structural changes such as defects, micro-stresses and local imperfections in Li_3N, which induce the α–β phase transition. In addition, ball milling reduces the crystallite size of Li_3N and increases the specific surface area (Table 1). All these characteristics make the milled Li_3N grains more reactive to hydrogen. However, this situation is reverted after prolonged hydriding, since the final hydrogen storage capacity of the m-LN sample does not reach the same value of commercial LN. This suggests that other mechanisms influence the absorption reaction at long times, which could be associated with the β-Li_3N fraction in the starting sample (Table 2).

Recently, it has been demonstrated that the hydrogenation of Li_3N is a more complex mechanism than that represented by reaction (1) and (2), involving non-stoichiometric phases [16–20]. In this context, the hydrogenation process of α-Li_3N occurs because of Li^+ ions migrate cooperatively through the cation vacancies within the lithium deficient Li_2N layers and interact with the hydrogen gas [16]. However, first-principles calculations have revealed that α-Li_3N and β-Li_3N have distinct Li^+ ion diffusion mechanisms: in α-Li_3N it occurs within the Li_2N plane, while in β-Li_3N it happens within the pure Li plane [29]. In addition, lower migration energy barriers for the Li^+ ion diffusion in α-Li_3N respect to β-Li_3N were reported. Therefore, increasing the Li^+ mobility is the basis of the mechanism of hydrogenation of Li_3N. The different crystallographic structure of α-Li_3N and β-Li_3N and the dissimilar Li^+ diffusion mobility could be responsible for the detrimental absorption behavior observed in milled-LN samples, which contain about 90% of β-Li_3N, respect to commercial LN that possesses 30% of β-Li_3N. In this sense, although the h-LN sample contains only α-Li_3N phase, hydrogen absorption behavior is affected by the microstructural modifications introduced as a consequence of the thermal treatment. Considering that these modifications affect Li diffusion, heating of commercial Li_3N under vacuum for 4 h has a negative effect on hydriding performance.

Combination of hydrogen absorption/desorption measurements and structural/microstructural characterizations by XRD, DSC, SEM and SSA suggest that ball milling induces both α to β-Li_3N phase transition and the modification of the Li_3N microstructure. The amount of β-Li_3N phase determines the kinetics of the hydrogenation at 200 °C and the hydrogen storage capacity in the milled Li_3N. The addition of Li_2O does not have any effect on the extension of the α to β-Li_3N phase transition and it acts as an inert component in the Li_3N–Li_2O starting mixture, with a hydrogen absorption kinetics that correlates with the amount of β-Li_3N phase in the sample as consequence of milling time. On the other hand, the thermal treatment favors the crystallite growth, influencing its reactivity with hydrogen. However, the microstructural changes in the starting samples showed a weaker effect on the hydrogen storage properties respect to the amount of β-Li_3N phase.

3.3. Hydriding/dehydriding behavior of Li_3N–LiH mixtures

From the above results, the as-received LN showed the higher hydrogen storage capacity with a gradual degradation of the hydrogen storage capacity under hydrogen cycling. The formation of NH_3 during dehydriding of $LiNH_2$ has been suggested to be the main reason for this depletion in the hydrogen storage properties [8–11]. For this reason, powders of LiH were added to Li_3N by milling to produce m-LN–LH2, m-LN20–LH2 and m-LNO–LH5 samples. Fig. 8 displays the XRD patterns of the different milled Li_3N–LiH mixtures. Minor changes are observed in the LN–LH mixtures respect to the starting LN samples (Fig. 1). The α-Li_3N and β-Li_3N (74%, Eq. (5)) phases are identified in the LN–LH2 mixture, while an almost

Fig. 7. Hydrogen absorption kinetics of: a) LN; b) m-LN5; c) m-LNO5. Isothermal absorption at 200 °C and 0.7 MPa of hydrogen pressure.
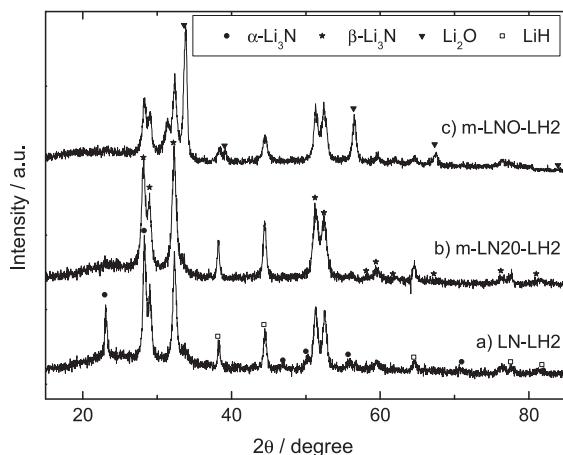
Fig. 8. PXRD patterns of: a) LN–LH2; b) m-LN20–LH2; c) m-LNO–LH5.

complete transition to the β-Li$_3$N phase is obtained in the LN20–LH2 sample. In contrast, after milling of the LNO–LH5 mixture the peak at $2\theta = 31.4°$ is clearly identified, indicating an interaction between Li$_2$O and LiH. FTIR measurement performed on the commercial Li$_2$O detect the presence of a band at 3677 cm^{-1}, that can be associated with Li(OH) (results not shown) [30]. This band is also clearly identified in the FTIR spectra of LNO–LH5, without the observation of the bands at 3180 and 3250 cm^{-1} or 3260 and 3315 cm^{-1} due to the presence of Li$_2$NH or LiNH$_2$, respectively [31]. Then, the diffraction peak observed at $2\theta = 31.4°$ originates in the interaction between of Li$_2$O containing LiOH with LiH.

Hydrogen absorption curves were measured for the different milled Li$_3$N–LiH mixtures (Fig. 9) under isothermal conditions (200 °C, pressure of H$_2$ = 0.7 MPa). The LN–LH2 sample absorbed 7.5 wt% of hydrogen in 2 h, whereas 4.5 and 2.7 wt% of hydrogen are incorporated in m-LN20–LH2 and m-LNO–LH5 samples, respectively. After this absorption step of 2 h, the hydrogen pressure was switched to 3.0 MPa to increase the hydrogen uptake (not shown). Final hydrogen storage capacities were 9.6, 7.0 and 4.2 wt% after 7 h for LN–LH, m-LN20–LH2 and m-LNO–LH5, respectively. After this first absorption, the samples were submitted to three successive cycles of desorption (250 °C, pressure of H$_2$ = 0.025 MPa)/absorption (200 °C, pressure of H$_2$ = 0.7 MPa for 2 h followed by 3.0 MPa for 7 h). All samples reached practically the same final reversible hydrogen uptake of about 3.5 wt% for LN–LH
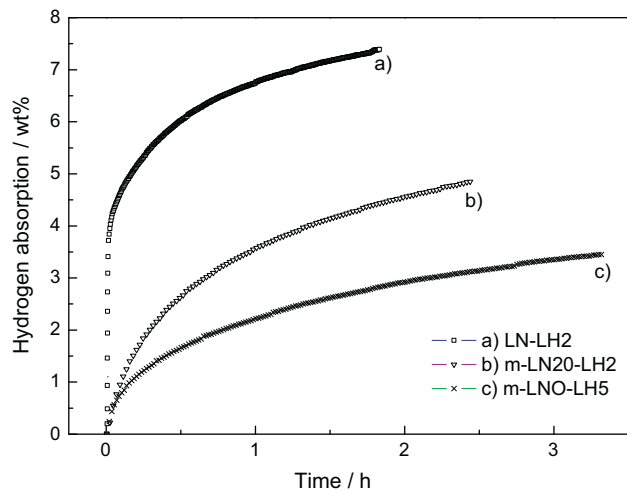

Fig. 9. Hydrogen absorption kinetics of: a) LN–LH2; b) m-LN20–LH2; c) m-LNO–LH5. Isothermal absorption at 200 °C and 0.7 MPa of hydrogen pressure.
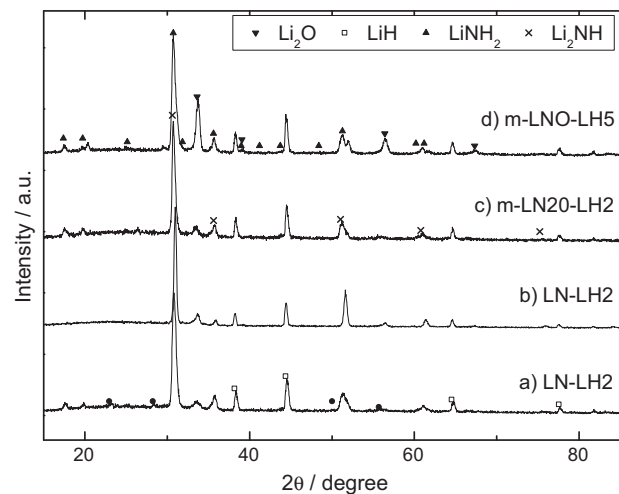

Fig. 10. PXRD patterns of: a) first absorption of LN–LH2; b) first desorption after absorption (a) of LN–LH2; c) 2nd cycle of absorption of m-LN20–LH2; d) 2nd cycle of absorption of m-LNO–LH5. Isothermal absorption at 200 °C (initial 0.7 MPa of hydrogen pressure for 2 h followed by 3.0 MPa of hydrogen for 7 h). Isothermal desorption at 250 °C (0.02 MPa of hydrogen pressure).

and 3.0 wt% for m-LN20–LH2 and m-LNO–LH5 samples, in spite of the dissimilar first absorption cycle.

PXRD patterns from Fig. 10 were used to identify the phases present in the samples after the first absorption cycle (LN–LH sample, curve a), third absorption cycle (LN–LH and LN20–LH2 samples, curves c and d) and first desorption cycle (LN–LH sample, curve b). The diffraction patterns reveal that for the three samples the main product of the hydriding is LiNH$_2$ and LiH, with minor amounts of Li$_2$NH. On the other hand, Li$_2$O is clearly identified in the samples LN–LH and LN20–LH2, probably due to both the crystallization of Li$_2$O present in the starting samples and the progressive oxidation of the samples during cycling/handling. In the case of m-LNO–LH5, minor amounts of Li$_4$NH seem to be formed during cycling [28]. The PXRD of the first desorption cycle (Fig. 10, curve b) shows only the presence of Li$_2$NH, LiH and Li$_2$O. These results were unequivocally corroborated by FTIR measurements.

By comparison of the hydriding/dehydriding behavior of the Li$_3$N samples with those where LiH was intentionally added, we can conclude that the main difference is associated with the stability of these samples under hydrogen cycling. This result demonstrates that the degradation of the Li$_3$N sample during hydrogen cycling due to the formation of NH$_3$ was reduced/eliminated by LiH addition, as was expected in accordance with previous works [8–11]. The differences observed in the first cycle in the presence of LiH manifest two factors that influence the hydriding kinetics: the presence of the β-Li$_3$N phase, which transforms during desorption cycling at 250 °C, and the microstructural modifications introduced by milling. For example, in the LN sample the content of β-Li$_3$N phase is 30%, while in the LN–LH sample is about 74%. In addition, the LN–LH sample was submitted to milling for 2 h to improve the mixing with LiH. Both factors affect the absorption rate in opposite ways, as it was analyzed for the Fig. 4. In the case of the m-LNO–LH5 sample, its low hydrogen storage capacity in the first cycle is also due to the presence of contamination in the starting Li$_2$O.

4. Conclusions

Different samples obtained from as-purchased Li$_3$N were analyzed to determine the role of the β-Li$_3$N phase, Li$_2$O and the thermal treatment of Li$_3$N on the hydrogen sorption properties. Combination of XRD, DSC, SEM and SSA studies were used to

understand the influence of the microstructure and structural changes on the hydrogen sorption kinetics.

The results of the present study demonstrate that as-received Li_3N displays the best behavior during the hydrogen absorption/desorption cycling. The milling procedure promotes the α to β structural transition in the commercial Li_3N and Li_3N–Li_2O samples, with the simultaneous refinement of the microstructure and local/surface modifications. These microstructural changes improve the absorption rate at short times under 0.7 MPa of hydrogen and 200 °C. However, the predominant factor during additional hydriding is the amount of β-Li_3N present in the sample. In comparison with α-Li_3N, the β-Li_3N phase retards the absorption rate with a detrimental effect on the total hydrogen storage capacity. No interaction between Li_2O and Li_3N was observed during milling and the hydrogen absorption behavior is dominated by the presence of the β-Li_3N phase. The Li_3N thermally treated at 400 °C exhibits an intermediate performance between as-received Li_3N and as-milled samples, without a clear beneficial effect of the annealing on the hydrogen sorption.

The addition of LiH to the commercial Li_3N, as-milled Li_3N and Li_3N–Li_2O mainly affects the hydrogen storage capacity in the first cycle and then the stability of the samples under cycling, with reversible hydrogen storage capacities of 3.0–3.5 wt% after three cycles. The hydrogen absorption/desorption behavior is mainly controlled by the amount of β-Li_3N formed during milling with an unappreciable effect of the microstructure at long times, both in the samples with and without LiH. The hydriding/dehydriding reaction was shown to be a complex process, as suggested by the identification of Li_4NH and a non-stoichiometric $Li_{2-x}NH_{1+x}$ phase under different experimental conditions.

References

[1] G. Walker, Solid-State Hydrogen Storage: Materials and Chemistry, Woodhead Publishing Ltd, England, 2008.
[2] R. Varin, T. Czujko, Z. Wronski, Nanomaterials for Solid State Hydrogen Storage, Springer, New York, 2009.
[3] A. Züttel, A. Borgschulte, L. Schlapbach, Hydrogen as a Future Energy Carrier, Wiley-VCH, Weinheim, 2008.
[4] M. Fichtner, Adv. Eng. Mater. 7 (2005) 443–455.
[5] W. Grochala, P.P. Edwards, Chem. Rev. 104 (2004) 1283–1315.
[6] P. Chen, Z. Xiong, J. Luo, J. Lin, K.L. Tan, Nature 420 (2002) 302–304.
[7] P. Chen, Z. Xiong, J. Luo, L. Lin, K. Tan, J. Phys. Chem. B 107 (2003) 10967–10970.
[8] T. Ichikawa, N. Hanada, S. Isobe, H. Leng, H. Fujii, J. Phys. Chem. B 108 (2004) 7887–7892.
[9] Y.H. Hu, E. Ruckenstein, J. Phys. Chem. A 107 (2003) 9737–9739.
[10] L. Shaw, W. Osborn, T. Markmaitree, X. Wan, J. Power Sources 177 (2008) 500–505.
[11] T. Ichikawa, H.Y. Leng, S. Isobe, N. Hanada, H. Fujii, J. Power Sources 159 (2006) 126–131.
[12] Y.H. Hu, E. Ruckenstein, Ind. Eng. Chem. Res. 43 (2004) 2464–2467.
[13] Y.H. Hu, N.Y. Yu, E. Ruckenstein, Ind. Eng. Chem. Res. 43 (2004) 4174–4177.
[14] Y.H. Hu, N.Y. Yu, E. Ruckenstein, Ind. Eng. Chem. Res. 44 (2005) 4304–4309.
[15] H.W. Langmi, S.D. Culligan, G.S. MacGrady, J. Power Sources 195 (2010) 2003–2007.
[16] W.I.F. David, M.O. Jones, D.H. Gregory, C.M. Jewell, S.R. Johnson, A. Walton, P.P. Edwards, J. Am. Chem. Soc. 129 (2007) 1594–1601.
[17] E. Weidner, D.J. Bull, I.L. Shabalin, S.G. Keens, M.T.F. Telling, D.K. Ross, Chem. Phys. Lett. 444 (2007) 76–79.
[18] D. Chandra, L. Joshua, W.-M. Chien, I. Gantan, K. Yvon, D. Phanon, R. Cerney, N. Penin, R. Cantelli, M. Latroche, DOE Hydrogen Program, FY 2009 Annual Progress Report, 477–482.
[19] A. Huq, J.W. Richardson, E.R. Maxey, D. Chandra, W.M. Chien, J. Phys. Chem. C 111 (2007) 10712–10717.
[20] D.J. Bull, E. Weidner, I.L. Shabalin, M.T.F. Telling, C.M. Jewell, D.H. Gregory, D.K. Ross, Phys. Chem. Chem. Phys. 12 (2010) 2089–2097.
[21] J.C. Crivello, M. Gupta, R. Černy, M. Latroche, D. Chandra, Phys. Rev. B 81 (2010) 104113.
[22] F. Zhang, Y. Wang, M.Y. Chou, Phys. Rev. B 82 (2010) 094112.
[23] J. Sangster, A.D. Pelton, J. Phase Equilib. 13 (1992) 291–296.
[24] D.H. Gregory, Coord. Chem. Rev. 215 (2001) 301–345.
[25] H.J. Beister, S. Haag, R. Kniep, K.S. Ner, K. Syassen, Angew. Chem. Int. Ed. 27 (1988) 1101–1103.
[26] A. Huq, J.W. Richardson, E.R. Maxey, D. Chandra, W.-M. Chien, J. Alloys Compd. 436 (2007) 256–260.
[27] P.P. Prosini, F. Cardellini, Electrochem. Commun. 4 (2002) 853–856.
[28] R. Marx, Z. Anorg, Allg. Chem. 623 (1997) 1912–1916.
[29] W. Li, G. Wu, M. Araújo, R. Scheicher, A. Blomqvist, R. Abuja, Z. Xiong, Y. Feng, P. Chen, Energy Env. Sci. 3 (2010) 1524–1531.
[30] S. Tanaka, M. Taniguchi, M. Nakatani, D. Yamaki, M. Yamawaki, J. Nucl. Mater. 218 (1995) 335–338.
[31] Y. Kojima, Y. Kawai, Chem. Commun. (2004) 2210–2211.